Production of high-orbital kaon excited states in the K^-p reaction

Ting-Yan Li,* Zi-Yue Bai,† and Xiang Liu‡

School of Physical Science and Technology, Lanzhou University, Lanzhou 730000, China, Lanzhou Center for Theoretical Physics, Key Laboratory of Theoretical Physics of Gansu Province, Key Laboratory of Quantum Theory and Applications of MoE, Gansu Provincial Research Center for Basic Disciplines of Quantum Physics, Lanzhou University, Lanzhou 730000, China, MoE Frontiers Science Center for Rare Isotopes, Lanzhou University, Lanzhou 730000, China, and Research Center for Hadron and CSR Physics, Lanzhou University and Institute of Modern Physics of CAS, Lanzhou 730000, China

(Received 16 June 2026; accepted 11 August 2026; published 25 August 2026)

In this work, a systematic investigation of the production of high-orbital-excitation kaons in K^-p reactions is carried out within an effective Lagrangian model. The relevant t-channel processes are constructed, and the model is calibrated using a single adjustable parameter determined from existing experimental data. With this parameter, the measured production cross sections for the $K_3^*(1780)$, $K_2(1820)$, $K_2(1770)$, and $K_4^*(2045)$ states are successfully reproduced. Employing the same framework, the production cross sections for other high-orbital kaons are predicted. The results indicate that these states possess sizable cross sections and exhibit characteristically forward-peaked angular distributions, which is a typical feature of t-channel exchange, highlighting their great potential for observation in future experiments.

DOI: 10.1103/14jg-wb6h

I. INTRODUCTION

Although numerous new hadronic states have been observed in collider experiments over the past two decades [1–6], it is important to recognize that meson-beam experiments have played a crucial role in establishing the main spectrum of light hadrons as listed in the Review of Particle Physics [7]. In recent years, combined with these observed new hadronic states, there have also been numerous phenomenological studies of how to produce them in meson beam experiments [8–11]. At present, the importance of meson beam experiments in the study of hadron spectroscopy should not be neglected; rather, it should be especially emphasized [12].

Generally, a meson beam is chosen as either a pion beam or a kaon beam. Pion-nucleon reactions can produce light mesons without strange quarks, while kaon-nucleon reactions can be applied mainly to produce light mesons with strange quarks. As indicated in the title of this work, excited-kaon production in kaon-nucleon reactions is the focus of our study.

The kaon family, a crucial subset of light hadrons distinguished by the presence of a strange quark, exhibits properties markedly different from those of light nonstrange mesons. For decades, meson-beam experiments have served as a primary tool for their study, yielding a wealth of experimental data. Examining the known kaon states, we find that low-lying kaons were discovered many decades ago. However, data for high-lying states are much more limited. A clear trend emerges from the experimental data on the resonance parameters—masses and widths—of these kaons: as the orbital quantum number increases, fewer experimental data are available. Consequently, the spectroscopic picture of the kaon family remains incomplete and requires further refinement.

Despite this incomplete picture, the recent discovery of two new kaon resonances, $K_3'(2120)$ and $K_4(2210)$ (highlighted in red in Fig. 1), by the COmmon Muon Proton Apparatus for Structure and Spectroscopy (COMPASS) Collaboration in 2025 via Kp scattering [13], has further enriched the spectrum. The newly observed $K_3'(2120)$ and $K_4(2210)$ belong to the $1F$ and $1G$ states, respectively. Other well-established high-orbital kaons, such as the $1D$ states $K_3^*(1780)$, $K_2(1820)$, $K_2(1770)$, and the $1F$ state $K_4^*(2045)$, have also been observed in meson-beam experiments, providing clear measurements of their production cross sections [14–18]. On the theoretical front, significant

*Contact author: lity2023@lzu.edu.cn
†Contact author: baiziyue@lzu.edu.cn
‡Contact author: xiangliu@lzu.edu.cn

Published by the American Physical Society under the terms of the Creative Commons Attribution 4.0 International license. Further distribution of this work must maintain attribution to the author(s) and the published article's title, journal citation, and DOI. Funded by SCOAP³.

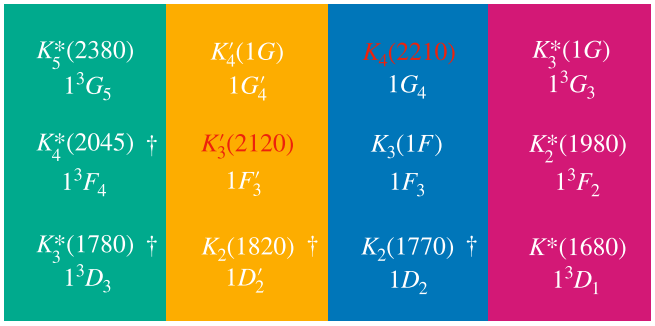

FIG. 1. A collection of high-orbital kaons. Two newly observed kaons, $K_3'(2120)$ and $K_4(2210)$, are marked in red, as reported by the COMPASS Collaboration in 2025 [13]. Four states marked with daggers have corresponding experimental cross-section data available for K^-p reactions.

progress has been made in modeling the mass spectrum via potential models and Regge trajectories [19,20], and in calculating decay properties using frameworks such as the quark pair creation (QPC) model and effective Lagrangian methods [21–23]. For clarity, the high-orbital kaon states considered in this work are summarized in Table I. The table lists their spin-parity quantum numbers, spectroscopic assignments, experimental status, and the interpretations adopted in the present calculation.

Although the present work focuses mainly on high-orbital kaon multiplets, the excited vector-kaon sector also deserves attention. The conventional $K^*(1410)$ and $K^*(1680)$ states are commonly associated predominantly with the 2^3S_1 and 1^3D_1 $q\bar{q}$ configurations, respectively [24]. In the present calculation, the production of the orbitally excited $K^*(1680)$ is explicitly included as part of the $1D$-wave multiplet.

In addition to these conventional states, the strange member of the light hybrid nonet may have the same observable quantum numbers $J^P = 1^-$ and may occur in a nearby mass region [25]. Its decay pattern is expected to differ from that of a conventional vector kaon; in particular, axial-kaon channels such as $K_1(1270)\pi$ and $K_1(1400)\pi$ may provide useful discriminating observables. Therefore, future production and decay data in the vector-kaon sector could test the conventional $q\bar{q}$ assignments, constrain possible conventional-hybrid mixing, and provide complementary constraints on phenomenological production models. A systematic treatment of this sector, including the relevant mixing and additional production mechanisms, is left for future work.

In stark contrast, the production mechanisms of these high-orbital kaons have received little theoretical attention. Their production dynamics thus represent a vital and underexplored area of study. This paper provides a brief overview of kaon production in meson-beam experiments, which provides an excellent platform for such investigations [12]. Future facilities, such as those planned at Japan Proton Accelerator Research Complex (J-PARC) and the potential meson-beam installation at High Intensity Heavy-ion Accelerator Facility (HIAF), underscore the continued relevance of this approach. Building on these experimental prospects and on established theoretical spectroscopy, in the following sections, we calculate the production cross sections for the discussed high-orbital kaons shown in Fig. 1. Our calculations are performed using a unified parameter set, based on the robust experimental data available for the $K_3^*(1780)$, $K_2(1820)$ and $K_2(1770)$ states.

The paper is organized as follows: following this Introduction, we present the effective Lagrangian model in Sec. II to investigate the production of the high-orbital kaons in the K^-p reaction. Numerical results and discussion are presented in Sec. III. In Sec. IV, we summarize the present work.

TABLE I. Summary of the high-orbital kaon states considered in this work. The labels $1L_J$ and $1L_J'$ denote the two physical states arising from the mixing of the 1^1L_J and 1^3L_J configurations.

	States	J^P	$n^{2S+1}L_J$	Status	Assignment
$1D$	$K_3^*(1780)$	3^-	1^3D_3	Established	$q\bar{q}$ meson
	$K_2(1770)$	2^-	$1D_2$	Established	
	$K_2(1820)$	2^-	$1D_2'$	Established	
	$K^*(1680)$	1^-	1^3D_1	Established	
$1F$	$K_4^*(2045)$	4^+	1^3F_4	Established	$q\bar{q}$ meson
	$K_3'(2120)$	3^+	$1F_3'$	Candidate	
	$K_3(1F)$	3^+	$1F_3$	Predicted	
	$K_2^*(1980)$	2^+	1^3F_2	Candidate	
$1G$	$K_5^*(2380)$	5^-	1^3G_5	Candidate	$q\bar{q}$ meson
	$K_4(2210)$	4^-	$1G_4$	Candidate	
	$K_4'(1G)$	4^-	$1G_4'$	Predicted	
	$K_3^*(1G)$	3^-	1^3G_3	Predicted	

II. FRAMEWORK FOR STUDYING HIGH-ORBITAL KAON PRODUCTION VIA THE K^-p REACTION

In this section, we present the theoretical foundation required for the subsequent calculations. The Feynman diagrams considered are shown in Fig. 2. Since the pole mass of the intermediate nucleon is well below the production threshold of the final-state kaon and proton, the contribution from the s-channel is highly suppressed. Moreover, the u-channel contribution is negligible because baryon-antibaryon decay modes of these high-orbital-excitation kaons are either kinematically disfavored or experimentally insignificant. Therefore, we adopt the effective Lagrangian model to calculate the corresponding t-channel amplitude. Since the two-body strong decays of the kaons in Fig. 1 have already been calculated by theorists, and their theoretical results are in good agreement with experimental data [20,23], we consider t-channel Feynman diagrams where the exchanged particles originate from kaon-containing decay channels.

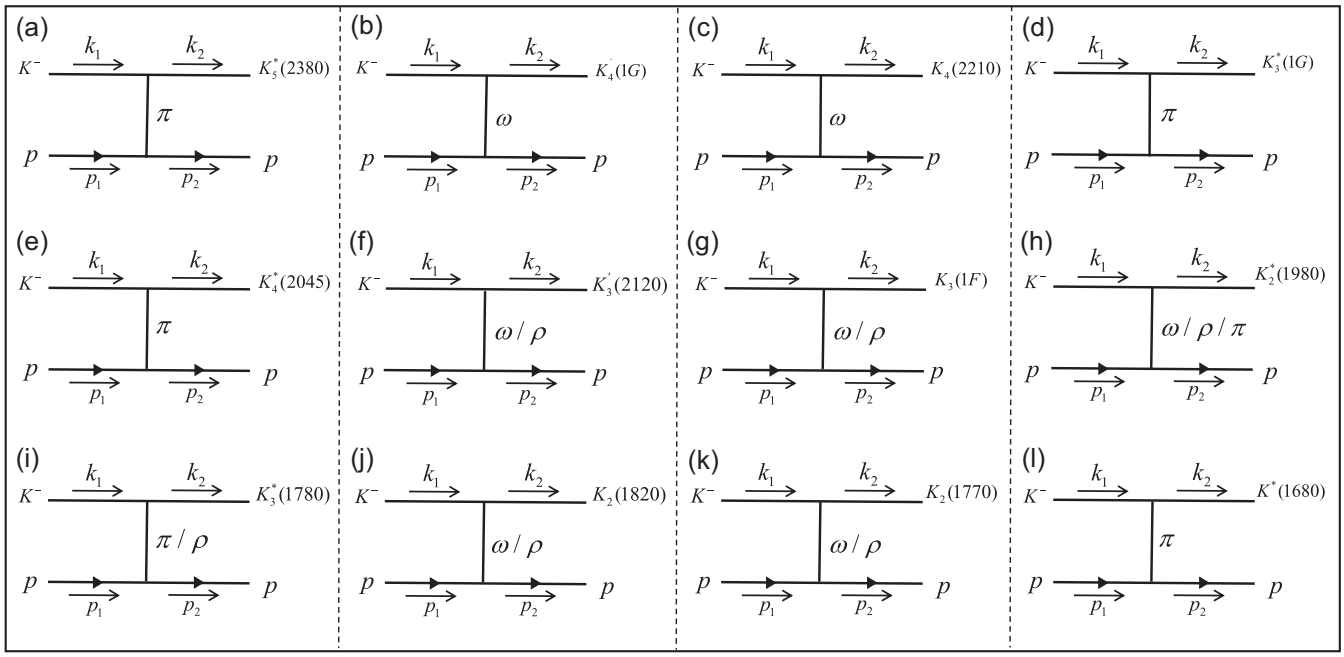

FIG. 2. Feynman diagrams for the $K^-p \to K_J + N$ reactions. Panels (a)–(l) correspond to the production of $K_5^*(2380)$, $K_4'(1G)$, $K_4(2210)$, $K_3^*(1G)$, $K_4^*(2045)$, $K_3'(2120)$, $K_3(1F)$, $K_2^*(1980)$, $K_3^*(1780)$, $K_2(1820)$, $K_2(1770)$, and $K^*(1680)$, respectively.

A. 1*D*-wave states

For the $1D$-wave states in Fig. 1, the $K_3^*(1780)$ corresponds to the 1^3D_3 state. The $K_3^*(1780)$ is established in the Particle Data Group (PDG) as a strange meson with $I(J^P) = 1/2(3^-)$ [7]. Its resonance parameters are listed with an average mass and width of 1779 ± 8 MeV and 161 ± 17 MeV, respectively. The mass of the $K_3^*(1780)$ has been measured in numerous production channels over several decades, beginning with its first observations in the 1970s [26–28]. The PDG average mass is derived from a series of experiments conducted in reactions such as $K^-p \to K^-\pi^+n$ and $K^+p \to K^0\pi^+p$ [26,29]. The dominant hadronic decay of the $K_3^*(1780)$ is $K\rho$ with a branching fraction of $(31 \pm 9)\%$, followed by $K^*(892)\pi$ ($(20 \pm 5)\%$) and $K\pi$ ($(18.8 \pm 1.0)\%$) [30]. The branching ratio for $\pi K_2^*(1430)$ is experimentally limited to $<16\%$ (CL $= 95\%$) [30]. Based on the theoretical predictions compiled in Ref. [23], the hadronic decay properties of the $K_3^*(1780)$ are further detailed. The dominant channel is ρK^*, which is followed by the ωK^* and πK channels.

The states $K_2(1770)$ and $K_2(1820)$ correspond to mixtures[1] of the 1^1D_2 and 1^3D_2 states. These two states share the same quantum numbers $I(J^P) = 1/2(2^-)$. The $K_2(1770)$ has a measured mass and width of 1773 ± 8 MeV and 186 ± 14 MeV, respectively. The $K_2(1820)$ is heavier and broader, with a mass of 1819 ± 12 MeV and a width of 264 ± 34 MeV [7]. Both states have been observed in complementary production processes. The $K_2(1770)$ was first established in K^-p scattering experiments, such as $K^-p \to K^-\omega p$ and $K^-p \to K^-2\pi p$, conducted at facilities such as Large Aperture Superconducting Solenoid (LASS) [17,31]. Its existence has been confirmed in modern analyses, notably in the decay $B^+ \to J/\psi\phi K^+$ by the LHCb Collaboration [32]. Similarly, the $K_2(1820)$ was also discovered in the LASS experiment through the $K^-\omega$ channel [17] and has been observed in the same $B^+ \to J/\psi\phi K^+$ decay by LHCb [32]. The $K_2(1770)$ primarily decays to $K\pi\pi$, $K^*(892)\pi$ and $K_2^*(1430)\pi$. The $K_2(1820)$, while sharing these dominant modes, also shows a significant branching fraction to $K\phi$, a channel not prominent for the $K_2(1770)$. In Ref. [20],[2] the strong decay widths of these two states as a function of the mixing angle are provided, and it is predicted that their mixing angle tends to be negative. The largest π-containing decay channels for both the $K_2(1770)$ and $K_2(1820)$ mesons are $K\rho$ and $K\omega$. Our calculated cross sections for these two states at $\theta_{1D} = -30°$ are in good agreement with the experimental data, as will be shown and discussed in a later section.

[1]Following Ref. [20], for $nL = 1D, 1F, 1G$, the mixing between the spin-singlet and spin-triplet kaon states is defined as $|K(nL)\rangle = \cos\theta_{nL}|n^1L_L\rangle + \sin\theta_{nL}|n^3L_L\rangle$ and $|K'(nL)\rangle = -\sin\theta_{nL}|n^1L_L\rangle + \cos\theta_{nL}|n^3L_L\rangle$. For the $1D$-wave, this convention gives $|K(1D)\rangle = |K_2(1770)\rangle$, $|K'(1D)\rangle = |K_2(1820)\rangle$. The same convention is adopted for the $1F$ and $1G$ mixed pairs.

[2]In Ref. [20], the decay channel written as $K\pi$ in the discussion of the $K_2(1770)$ decay should read $K_1\pi$; this appears to be a typographical error.

The $K^*(1680)$ corresponds to the 1^3D_1 state. The $K^*(1680)$ has an average mass and width of 1718 ± 18 MeV and 320 ± 110 MeV. It was first observed in the 1970s and 1980s in formation experiments such as $K^-p \to K^-\pi^+n$ and $K^-p \to \bar{K}^0\pi^+\pi^-n$ conducted with the LASS spectrometer [29,30]. More recently, it was also observed in the decay $B^+ \to J/\psi\phi K^+$ by the LHCb Collaboration with a significance of 8.5σ [32]. Its dominant decays are to $K\pi$ (~39%), $K\rho$ (~31%), and $K^*(892)\pi$ (~30%). The strong decay widths of this state are predicted in Ref. [20].

To study the four production reactions involving the $1D$-wave strange-meson states, we first construct the effective interaction Lagrangians associated with the upper vertices in Fig. 2. These vertices describe the couplings of the produced strange mesons to the incident kaon and the exchanged light meson. The interaction structures are chosen to satisfy Lorentz covariance and to be consistent with the spin-parity quantum numbers of the participating mesons.

Based on the decay properties summarized in Refs. [20,23], the exchanged mesons retained for the production of the individual states are selected as follows: for the $K_3^*(1780)$, both π and ρ exchanges are included, whereas the η-exchange contribution is neglected because of its very small production cross section. For the $K_2(1820)$ and $K_2(1770)$, whose important decay modes involve vector mesons, only ρ and ω exchanges are considered. The η-exchange contribution to the $K_2(1820)$ production is again found to be negligible. For the $K^*(1680)$, the large branching fractions into $K\pi$ and $K\rho$ motivate the consideration of both pseudoscalar- and vector-meson exchange mechanisms. However, since the ρ-exchange contribution is numerically very small, only the π-exchange contribution is retained in the final results.

For the spin-three state $K_3^*(1780)$, represented by the rank-three tensor field $K_3^{*,\mu\nu\rho}$, the $K\pi$ interaction contains three derivatives, as required by the angular-momentum structure of the vertex. The corresponding effective Lagrangian is written as

$$\mathcal{L}_{K_3^*(1780)K\pi} = g_{K_3^*(1780)K\pi} K_3^{*+,\mu\nu\rho}[K^-(\partial_\mu\partial_\nu\partial_\rho\pi^0) - \pi^0(\partial_\mu\partial_\nu\partial_\rho K^-)], \quad (1)$$

where $g_{K_3^*(1780)K\pi}$ denotes the effective coupling constant of the $K_3^*(1780)K\pi$ vertex.

The interaction of the $K_3^*(1780)$ with a kaon and a vector ρ meson is constructed with the Levi-Civita tensor. This form accounts for the parity properties of the $K_3^*(1780)K\rho$ vertex and is given by

$$\mathcal{L}_{K_3^*(1780)K\rho} = g_{K_3^*(1780)K\rho}\epsilon^{\mu\nu\rho\sigma} K_3^{*+,\mu\alpha\beta}(\partial_\nu\rho_\rho^0) \times (\partial^\alpha\partial^\beta\partial_\sigma K^-). \quad (2)$$

The physical states $K_2(1820)$ and $K_2(1770)$ have the same quantum numbers $I(J^P) = 1/2(2^-)$. Since they are mixtures of the 1^3D_2 and 1^1D_2 configurations, the same Lorentz structures are adopted for their couplings to $K\omega$ and $K\rho$, while their effective coupling constants are treated independently.

For the $K_2(1820)$ state, the relevant interaction Lagrangians are

$$\mathcal{L}_{K_2(1820)\omega K} = g_{K_2(1820)\omega K} K_2^{+,\alpha\beta}\omega_\alpha\partial_\beta K^-, \quad (3)$$

and

$$\mathcal{L}_{K_2(1820)\rho K} = g_{K_2(1820)\rho K} K_2^{+,\alpha\beta}\rho_\alpha^0\partial_\beta K^-. \quad (4)$$

Analogously, the interactions of the $K_2(1770)$ state with the ωK and ρK channels are described by

$$\mathcal{L}_{K_2(1770)\omega K} = g_{K_2(1770)\omega K} K_2^{+,\alpha\beta}\omega_\alpha\partial_\beta K^-, \quad (5)$$

and

$$\mathcal{L}_{K_2(1770)\rho K} = g_{K_2(1770)\rho K} K_2^{+,\alpha\beta}\rho_\alpha^0\partial_\beta K^-. \quad (6)$$

For the vector state $K^*(1680)$, the $K^*(1680)K\pi$ interaction is described by the conventional derivative coupling among one vector and two pseudoscalar mesons. The corresponding Lagrangian reads

$$\mathcal{L}_{K^*(1680)K\pi} = g_{K^*(1680)K\pi} K^{*0,\alpha}(K^-\partial_\alpha\pi^+ - \pi^+\partial_\alpha K^-). \quad (7)$$

We next specify the interaction Lagrangians at the lower vertices of Fig. 2, which describe the couplings of the exchanged light mesons to the nucleons. For the vector-meson exchanges, both vector and tensor couplings are included. The corresponding phenomenological Lagrangians are taken from Refs. [33,34] and are written as

$$\mathcal{L}_{\omega NN} = g_{\omega NN}\bar{N}\gamma_\mu\omega^\mu N + \frac{f_{\omega NN}}{4m_p}\bar{N}\sigma_{\mu\nu}(\partial^\mu\tilde{\omega}^\nu - \partial^\nu\tilde{\omega}^\mu)N, \quad (8)$$

and

$$\mathcal{L}_{\rho NN} = g_{\rho NN}\bar{N}\gamma_\mu\rho^\mu N + \frac{f_{\rho NN}}{4m_p}\bar{N}\sigma_{\mu\nu}(\partial^\mu\rho^\nu - \partial^\nu\rho^\mu)N. \quad (9)$$

For the pseudoscalar-pion exchange, we employ the standard pseudovector πNN interaction,

$$\mathcal{L}_{\pi NN} = \frac{f_{\pi NN}}{m_\pi}\bar{N}\gamma_\mu\gamma^5\partial^\mu\tilde{\pi}N. \quad (10)$$

Here, N denotes the nucleon field, while g_{VNN} and f_{VNN} represent, respectively, the vector coupling constants for the vector meson $V = \rho, \omega$. The quantities m_p and m_π denote the proton and pion masses, respectively.

Combining the upper three-meson vertices with the meson propagators and the lower meson-nucleon vertices, we obtain the tree-level t-channel amplitudes for the four production reactions. We define the four-momentum transfer as $q = p_1 - p_2 = k_2 - k_1$ and the Mandelstam variable as $t = q^2$. The momenta k_1 and p_1 denote the momenta of the incident kaon and nucleon, respectively, whereas k_2 and p_2 denote those of the produced strange meson and the outgoing nucleon. The phenomenological function $F_t(q)$ accounts for the finite-size effects at the interaction vertices.

For the $K_3^*(1780)$ production through pion exchange, the amplitude is

$$i\mathcal{M}_{K_3^*(1780)\pi K} = g_{K_3^*(1780)\pi K}\frac{f_{\pi NN}}{m_\pi}\bar{u}(p_2)\gamma_\alpha\gamma_5 u(p_1)q^\alpha\frac{i}{t-m_\pi^2}\epsilon^{*,\mu\nu\rho}(k_2)(q_\mu q_\nu q_\rho + k_{1\mu}k_{1\nu}k_{1\rho})F_t(q). \tag{11}$$

The corresponding ρ-exchange amplitude is

$$i\mathcal{M}_{K_3^*(1780)\rho K} = -g_{K_3^*(1780)\rho K}\varepsilon^{\mu\nu\rho\sigma}\epsilon^*_{\mu\alpha\beta}(k_2)\frac{-i(g^\mu_\alpha + q^\mu q_\alpha/m_\rho^2)}{t-m_\rho^2}\bar{u}(p_2)\left[g_{\rho NN}\gamma_\xi - \frac{if_{\rho NN}}{2m_p}\sigma_{\delta\xi}q^\delta\right]u(p_1)q_\nu k_1^\alpha k_1^\beta k_{1\sigma}\times F_t(q). \tag{12}$$

For the $K_2(1820)$ production, the ω-exchange contribution is given by

$$i\mathcal{M}_{K_2(1820)\omega K} = ig_{K_2(1820)\omega K}\bar{u}(p_2)\left(g_{\omega NN}\gamma_\mu - \frac{if_{\omega NN}}{2m_p}\sigma_{\nu\mu}q^\nu\right)u(p_1)\epsilon^{*,\alpha\beta}(k_2)k_{1\beta}\frac{-i(g^\mu_\alpha + q^\mu q_\alpha/m_\omega^2)}{t-m_\omega^2}F_t(q). \tag{13}$$

Likewise, the ρ-exchange amplitude for the $K_2(1820)$ production reads

$$i\mathcal{M}_{K_2(1820)\rho K} = ig_{K_2(1820)\rho K}\bar{u}(p_2)\left(g_{\rho NN}\gamma_\mu - \frac{if_{\rho NN}}{2m_p}\sigma_{\nu\mu}q^\nu\right)u(p_1)\epsilon^{*,\alpha\beta}(k_2)k_{1\beta}\frac{-i(g^\mu_\alpha + q^\mu q_\alpha/m_\rho^2)}{t-m_\rho^2}F_t(q). \tag{14}$$

The $K_2(1770)$ amplitudes have the same Lorentz structures as those of the $K_2(1820)$, but involve the coupling constants associated with the $K_2(1770)$ state. The ω-exchange amplitude is

$$i\mathcal{M}_{K_2(1770)\omega K} = ig_{K_2(1770)\omega K}\bar{u}(p_2)\left(g_{\omega NN}\gamma_\mu - \frac{if_{\omega NN}}{2m_p}\sigma_{\nu\mu}q^\nu\right)u(p_1)\epsilon^{*,\alpha\beta}(k_2)k_{1\beta}\frac{-i(g^\mu_\alpha + q^\mu q_\alpha/m_\omega^2)}{t-m_\omega^2}F_t(q), \tag{15}$$

whereas the corresponding ρ-exchange amplitude is

$$i\mathcal{M}_{K_2(1770)\rho K} = ig_{K_2(1770)\rho K}\bar{u}(p_2)\left(g_{\rho NN}\gamma_\mu - \frac{if_{\rho NN}}{2m_p}\sigma_{\nu\mu}q^\nu\right)u(p_1)\epsilon^{*,\alpha\beta}(k_2)k_{1\beta}\frac{-i(g^\mu_\alpha + q^\mu q_\alpha/m_\rho^2)}{t-m_\rho^2}F_t(q). \tag{16}$$

Finally, the $K^*(1680)$ production is dominated by the pion-exchange mechanism. Its tree-level amplitude is expressed as

$$i\mathcal{M}_{K^*(1680)\pi K} = -g_{K^*(1680)\pi K}\frac{f_{\pi NN}}{m_\pi}\bar{u}(p_2)\gamma_\mu\gamma_5 u(p_1)q^\mu\frac{i}{t-m_\pi^2}\epsilon^{*,\alpha}(k_2)(q_\alpha + k_{1\alpha})F_t(q). \tag{17}$$

In the above expressions, $\epsilon^{\mu\nu\rho}(k_2)$, $\epsilon^{\mu\nu}(k_2)$, and $\epsilon^{\mu}(k_2)$ denote the polarization tensor or polarization vector of the produced spin-three, spin-two, and spin-one strange mesons, respectively. These amplitudes constitute the basic ingredients used below to calculate the total and differential production cross sections.

B. 1F-wave states

The $K_4^*(2045)$ is assigned as the 1^3F_4 state with $I(J^P) = 1/2(4^+)$ [7]. The $K_4^*(2045)$ is given an average mass and width of 2048^{+8}_{-9} MeV and 199^{+27}_{-19} MeV, respectively [7]. It has been observed in several production channels. The most precise recent measurement comes from the Beijing Spectrometer III (BESIII) experiment via $J/\psi \to K^+K^-\pi^0$, reporting a mass of $2090 \pm 9^{+11}_{-29}$ MeV [35]. Earlier studies in the 1980s, such as the LASS experiment using the reaction $K^-p \to K^-\pi^+n$ at 11 GeV/c, were crucial for its initial identification and the determination of its quantum numbers [36,37]. The $K_4^*(2045)$ predominantly decays into hadronic final states. The $K\pi$ channel has a branching

fraction of $(9.9 \pm 1.2)\%$, while the $K^*(892)\pi\pi$ and $\rho K\pi$ modes have comparable strengths of $(9 \pm 5)\%$ and $(5.7 \pm 3.2)\%$, respectively [18,29]. The theoretical decay pattern of the $K_4^*(2045)$ is calculated in Ref. [23]. The dominant mode for the $K_4^*(2045)$ is $K^*\rho$. Other significant channels include ωK^*, πK^*, $K\rho$, and πK.

The $K_3'(2120)$ and $K_3(1F)$ are mixtures of the 1^3F_3 and 1^1F_3 states. The COMPASS Collaboration reported the observation of two new strange mesons in 2025 via the scattering reaction $K^-p \to K^-\pi^+\pi^-p$ [13]. The observed states are the $K_3'(2120)$ and $K_4(2210)$, with masses and widths of $2119 \pm 13^{+45}_{-12}$ MeV, $270 \pm 30^{+40}_{-30}$ MeV, and $2210 \pm 40^{+80}_{-30}$ MeV, $250 \pm 70^{+50}_{-70}$ MeV, respectively. The $K_3(1F)$ is the partner state of the $K_3'(2120)$, and has not been observed experimentally. The mass and strong decays of the $K_3'(2120)$ and $K_3(1F)$ are calculated in Ref. [23]. The mass and total decay width for the $K_3(1F)$ are calculated to be 2066 MeV and 248 MeV, respectively [23]. While for $K_3'(2120)$, its total decay width is 277 MeV. The latter is in good agreement with the experimental width of $270 \pm 30^{+40}_{-30}$ MeV reported by the COMPASS Collaboration [13]. The decay of the $K_3(1F)$ is dominated by the Ka_2 channel. Other significant channels include ρK^* and ρK_1. The $K_3'(2120)$ decays mainly to $\pi K_3^*(1780)$ and πK_2^*. Channels such as ρK^* and $K\rho$ are also present but with smaller branching fractions.

The $K_2^*(1980)$ state corresponds to the 1^3F_2 state. The PDG lists its average mass and width as 1990^{+60}_{-50} MeV and 348^{+50}_{-30} MeV, respectively [7]. This state has been observed in multiple production channels. The most recent and precise measurement comes from the BESIII experiment via the decay $\psi(2S) \to K^+K^-\eta$, reporting a mass of 2046^{+17+67}_{-16-15} MeV [38]. An earlier measurement by the LASS Collaboration, using the reaction $K^-p \to K^0\pi^+\pi^-n$ at 11 GeV/c, found a mass of $1973 \pm 8 \pm 25$ MeV [30]. A signal consistent with the $K_2^*(1980)$ was also reported by LHCb in an amplitude analysis of $B^+ \to J/\psi\phi K^+$ decays [32], although a later analysis with higher statistics could not confirm it with significant certainty. The primary decay modes of the $K_2^*(1980)$ include $K_1(1270)\pi$, $K_2(1770)\pi$, Ka_1, Kb_1, and Kh_1, as listed in Ref. [20].

To study the four production reactions involving the $1F$-wave strange-meson states, we construct the effective interaction Lagrangians associated with the upper vertices in Fig. 2. These vertices describe the couplings of the produced strange mesons to the incident kaon and the exchanged light meson. As in the discussion of the $1D$-wave states, the interaction structures are chosen to satisfy Lorentz covariance and to be consistent with the spin-parity quantum numbers of the participating mesons. The meson-nucleon interactions at the lower vertices are the same as those introduced above and are taken from Refs. [33,34].

Based on the decay properties given in Refs. [20,23], we examine the possible t-channel exchange mechanisms for the individual $1F$-wave states and retain the numerically relevant contributions. For the $K_4^*(2045)$ production, the pion-exchange mechanism gives the dominant contribution, while the ρ-, ω-, and b_1-exchange contributions are found to be very small. Therefore, only the π exchange is retained. For the two spin-three states, the $K_3'(2120)$ and $K_3(1F)$, the ρ- and ω-exchange mechanisms are included. The a_1-exchange contribution to the $K_3'(2120)$ production and the b_1-exchange contribution to the $K_3(1F)$ production are numerically negligible. For the $K_2^*(1980)$ production, although the axial-vector channels such as Ka_1, Kb_1, and Kh_1 can have sizable decay fractions, the corresponding exchange contributions to the production cross section are strongly suppressed. By contrast, the $K\pi$ channel leads to the dominant production contribution. For completeness, the $K_2^*(1980)K\omega$ and $K_2^*(1980)K\rho$ interactions are also listed below to document the vector-meson exchange mechanisms examined in the calculation.

For the spin-four state $K_4^*(2045)$, represented by the rank-four tensor field $K_4^{*,\mu\nu\rho\sigma}$, the $K\pi$ interaction contains four derivatives, as required by the angular-momentum structure of the vertex. The corresponding effective Lagrangian is written as

$$\mathcal{L}_{K_4^*(2045)\pi K} = g_{K_4^*(2045)\pi K} K_4^{*+,\mu\nu\rho\sigma}[K^-(\partial_\mu\partial_\nu\partial_\rho\partial_\sigma\pi^0) + \pi^0(\partial_\mu\partial_\nu\partial_\rho\partial_\sigma K^-)]. \tag{18}$$

The physical states $K_3'(2120)$ and $K_3(1F)$ are mixtures of the 1^3F_3 and 1^1F_3 configurations. Since they have the same spin-parity quantum numbers, the same Lorentz structures are adopted for their couplings to the $K\omega$ and $K\rho$ channels, while the corresponding effective coupling constants are treated independently. For the $K_3'(2120)$ state, the relevant interaction Lagrangians are

$$\mathcal{L}_{K_3'(2120)\omega K} = g_{K_3'(2120)\omega K} K_3'^{+,\alpha\beta\gamma}\omega_\alpha\partial_\beta\partial_\gamma K^-, \tag{19}$$

and

$$\mathcal{L}_{K_3'(2120)\rho K} = g_{K_3'(2120)\rho K} K_3'^{+,\alpha\beta\gamma}\rho_\alpha^0\partial_\beta\partial_\gamma K^-. \tag{20}$$

Analogously, the interactions of the $K_3(1F)$ state with the ωK and ρK channels are described by

$$\mathcal{L}_{K_3(1F)\omega K} = g_{K_3(1F)\omega K} K_3^{+,\alpha\beta\gamma}\omega_\alpha\partial_\beta\partial_\gamma K^-, \tag{21}$$

and

$$\mathcal{L}_{K_3(1F)\rho K} = g_{K_3(1F)\rho K} K_3^{+,\alpha\beta\gamma}\rho_\alpha^0\partial_\beta\partial_\gamma K^-. \tag{22}$$

For the spin-two state $K_2^*(1980)$, the interactions with a kaon and a vector meson are constructed using

the Levi-Civita tensor. The corresponding effective Lagrangians are

$$\mathcal{L}_{K_2^*(1980)\omega K} = g_{K_2^*(1980)\omega K}\epsilon^{\mu\nu\lambda\sigma}K^{*+}_{2,\mu\alpha}(\partial_\nu\omega_\lambda)\partial_\sigma\partial^\alpha K^-, \quad (23)$$

and

$$\mathcal{L}_{K_2^*(1980)\rho K} = g_{K_2^*(1980)\rho K}\epsilon^{\mu\nu\lambda\sigma}K^{*+}_{2,\mu\alpha}(\partial_\nu\rho^0_\lambda)\partial_\sigma\partial^\alpha K^-. \quad (24)$$

The $K_2^*(1980)K\pi$ interaction contains two derivatives and is written as

$$\mathcal{L}_{K_2^*(1980)\pi K} = g_{K_2^*(1980)\pi K}K_2^{*+,\alpha\beta}[K^-(\partial_\alpha\partial_\beta\pi^0) + \pi^0(\partial_\alpha\partial_\beta K^-)]. \quad (25)$$

Combining the upper three-meson vertices with the exchanged-meson propagators and the lower meson-nucleon vertices, we obtain the tree-level t-channel amplitudes for the production of the $1F$-wave states. The definitions $q = p_1 - p_2 = k_2 - k_1$ and $t = q^2$ follow those introduced above, and the phenomenological form factor $F_t(q)$ is included at each t-channel exchange vertex.

For the $K_4^*(2045)$ production through pion exchange, the amplitude is

$$i\mathcal{M}_{K_4^*(2045)\pi K} = ig_{K_4^*(2045)\pi K}\frac{f_{\pi NN}}{m_\pi}\epsilon^{*,\mu\nu\rho\sigma}(k_2)q^\alpha\bar{u}(p_2)\gamma_\alpha\gamma_5 u(p_1)\frac{i}{t-m_\pi^2}(q_\mu q_\nu q_\rho q_\sigma + k_{1\mu}k_{1\nu}k_{1\rho}k_{1\sigma})F_t(q). \quad (26)$$

For the $K_3'(2120)$ production, the ω-exchange contribution is given by

$$i\mathcal{M}_{K_3'(2120)\omega K} = g_{K_3'(2120)\omega K}\bar{u}(p_2)\left(g_{\omega NN}\gamma_\mu - \frac{if_{\omega NN}}{2m_p}\sigma_{\nu\mu}q^\nu\right)u(p_1)\frac{-i(g^\mu{}_\alpha + q^\mu q_\alpha/m_\omega^2)}{t-m_\omega^2}\epsilon^{*,\alpha\beta\gamma}(k_2)k_{1\beta}k_{1\gamma}F_t(q), \quad (27)$$

while the corresponding ρ-exchange amplitude reads

$$i\mathcal{M}_{K_3'(2120)\rho K} = g_{K_3'(2120)\rho K}\bar{u}(p_2)\left(g_{\rho NN}\gamma_\mu - \frac{if_{\rho NN}}{2m_p}\sigma_{\nu\mu}q^\nu\right)u(p_1)\frac{-i(g^\mu{}_\alpha + q^\mu q_\alpha/m_\rho^2)}{t-m_\rho^2}\epsilon^{*,\alpha\beta\gamma}(k_2)k_{1\beta}k_{1\gamma}F_t(q). \quad (28)$$

The $K_3(1F)$ amplitudes have the same Lorentz structures as those of the $K_3'(2120)$ state, but involve the coupling constants associated with the $K_3(1F)$ state. The ω-exchange amplitude is

$$i\mathcal{M}_{K_3(1F)\omega K} = g_{K_3(1F)\omega K}\bar{u}(p_2)\left(g_{\omega NN}\gamma_\mu - \frac{if_{\omega NN}}{2m_p}\sigma_{\nu\mu}q^\nu\right)u(p_1)\frac{-i(g^\mu{}_\alpha + q^\mu q_\alpha/m_\omega^2)}{t-m_\omega^2}\epsilon^{*,\alpha\beta\gamma}(k_2)k_{1\beta}k_{1\gamma}F_t(q), \quad (29)$$

whereas the corresponding ρ-exchange contribution is

$$i\mathcal{M}_{K_3(1F)\rho K} = g_{K_3(1F)\rho K}\bar{u}(p_2)\left(g_{\rho NN}\gamma_\mu - \frac{if_{\rho NN}}{2m_p}\sigma_{\nu\mu}q^\nu\right)u(p_1)\frac{-i(g^\mu{}_\alpha + q^\mu q_\alpha/m_\rho^2)}{t-m_\rho^2}\epsilon^{*,\alpha\beta\gamma}(k_2)k_{1\beta}k_{1\gamma}F_t(q). \quad (30)$$

The vector-meson exchange amplitudes examined for the $K_2^*(1980)$ production are given. The ω-exchange contribution is

$$i\mathcal{M}_{K_2^*(1980)\omega K} = -ig_{K_2^*(1980)\omega K}\epsilon^{\mu\nu\lambda\sigma}\epsilon^*_{\mu\alpha}(k_2)q_\nu k_{1\sigma}k_1^\alpha\bar{u}(p_2)\left(g_{\omega NN}\gamma_\xi - \frac{if_{\omega NN}}{2m_p}\sigma_{\delta\xi}q^\delta\right)u(p_1)\frac{-i(g^\xi{}_\lambda + q^\xi q_\lambda/m_\omega^2)}{t-m_\omega^2}F_t(q), \quad (31)$$

and the ρ-exchange contribution is

$$i\mathcal{M}_{K_2^*(1980)\rho K} = -ig_{K_2^*(1980)\rho K}\epsilon^{\mu\nu\lambda\sigma}\epsilon^*_{\mu\alpha}(k_2)q_\nu k_{1\sigma}k_1^\alpha \times \bar{u}(p_2)\left(g_{\rho NN}\gamma_\xi - \frac{if_{\rho NN}}{2m_p}\sigma_{\delta\xi}q^\delta\right)u(p_1) \times \frac{-i(g^\xi{}_\lambda + q^\xi q_\lambda/m_\rho^2)}{t-m_\rho^2}F_t(q). \quad (32)$$

The $K_2^*(1980)$ production also retains the dominant pion-exchange contribution. The corresponding amplitude is

$$i\mathcal{M}_{K_2^*(1980)\pi K} = -ig_{K_2^*(1980)\pi K}\frac{f_{\pi NN}}{m_\pi}\epsilon^{*,\alpha\beta}(k_2)(q_\alpha q_\beta + k_{1\alpha}k_{1\beta}) \times \frac{i}{t-m_\pi^2}\bar{u}(p_2)\gamma_\mu\gamma_5 u(p_1)q^\mu F_t(q). \quad (33)$$

In the above expressions, $\epsilon^{\mu\nu\rho\sigma}(k_2)$, $\epsilon^{\mu\nu\rho}(k_2)$, and $\epsilon^{\mu\nu}(k_2)$ denote the polarization tensors of the produced spin-four, spin-three, and spin-two strange mesons, respectively. These amplitudes provide the ingredients required to evaluate the total and differential cross sections for the $1F$-wave states.

C. 1G-wave states

The $K_5^*(2380)$ is a candidate for the 1^3G_5 state with $I(J^P) = 1/2(5^-)$ [7]. Its experimental status remains to be confirmed. Its reported mass and width are 2382 ± 24 MeV and 180 ± 50 MeV, respectively [7]. To date, this state has only been observed in the LASS analysis of the reaction $K^-p \to K^-\pi^+n$ [37]. The only experimentally established two-body decay mode is $K\pi$, with a branching fraction of $(6.1 \pm 1.2)\%$, while theoretical calculations predict a rich decay pattern with numerous allowed open channels, owing to its relatively high mass and large spin. The two largest predicted channels are $K^*a_2(1320)$ and $\rho K_2^*(1430)$. Other important modes include ρK^*, $K^*f_2(1270)$, ωK_2^*, and Kb_1 [23].

The $K_4'(1G)$ and $K_4(2210)$ are mixtures of the 1^3G_4 and 1^1G_4 states. Their masses and strong decay properties were investigated in Ref. [23]. The decay of $K_4(2210)$ is dominated by the Ka_2 channel, with a branching fraction of 22.7% and a partial width of 26.1 MeV. Other notable channels include ρK_1 and ρK^*. In contrast, the predicted mass and total width of the as-yet-unobserved $K_4'(1G)$ are 2306 MeV and 161 MeV, respectively. Its important decay modes include $\pi K_3^*(1780)$, $\pi K_4^*(2045)$, πK_2^*, ρK^*, and ρK.

The $K_3^*(1G)$ is assigned as the 1^3G_3 state and has not yet been observed experimentally. We studied its mass and strong decay properties using the modified Godfrey-Isgur model and the QPC model, and the parameters are given in Ref. [23]. Its predicted mass and total width are 2305 MeV and 412.04 MeV, respectively. The dominant decay modes are expected to be $K_2(1770)\pi$, $K_2(1820)\pi$, $K\pi_2$, and $K\eta_2$. The $K_1\rho$, $K^*\rho$, and Kb_1 channels also provide sizable contributions.

To study the production of the four $1G$-wave kaon states, we construct the effective interaction Lagrangians associated with the upper vertices in Fig. 2. These vertices describe the couplings of the produced strange mesons to the incident kaon and the exchanged light meson. As in the discussions of the $1D$- and $1F$-wave states, the interaction structures are chosen to satisfy Lorentz covariance and to be consistent with the spin-parity quantum numbers of the participating mesons. The meson-nucleon interactions at the lower vertices are the same as those introduced above.

Based on the decay properties obtained in Ref. [23], we examine the possible t-channel exchange mechanisms and retain the numerically relevant contributions. It should be emphasized that a sizable decay branching fraction does not necessarily imply a dominant production contribution, since the exchanged-meson propagator, the meson-nucleon coupling, and the momentum structure of the vertex also affect the production amplitude. For the $K_5^*(2380)$ production, the pion-exchange mechanism provides the dominant contribution, whereas the ρ-, ω-, b_1-, and h_1-exchange contributions are numerically negligible. Therefore, only the π exchange is retained. For the $K_4'(1G)$ and $K_4(2210)$ states, only the ω-exchange mechanism is considered, because the corresponding ρ-exchange contributions are strongly suppressed. For the $K_3^*(1G)$ production, although the axial-vector channels such as Ka_1, Kb_1, and Kh_1 can have sizable decay fractions, their exchange contributions to the production cross section are small. By contrast, the $K\pi$ channel leads to the dominant production contribution. Therefore, only the pion-exchange mechanism is retained for the $K_3^*(1G)$ state.

For the spin-five state $K_5^*(2380)$, represented by the rank-five tensor field $K_5^{*,\alpha\beta\gamma\delta\sigma}$, the $K\pi$ interaction contains five derivatives, as required by the angular-momentum structure of the vertex. The corresponding effective Lagrangian is written as

$$\mathcal{L}_{K_5^*(2380)\pi K} = g_{K_5^*(2380)\pi K}K_5^{*+,\alpha\beta\gamma\delta\sigma}[K^-(\partial_\alpha\partial_\beta\partial_\gamma\partial_\delta\partial_\sigma\pi^0) - \pi^0(\partial_\alpha\partial_\beta\partial_\gamma\partial_\delta\partial_\sigma K^-)]. \quad (34)$$

The physical states $K_4'(1G)$ and $K_4(2210)$ have the same spin-parity quantum numbers. Since they arise from the mixing of the 1^3G_4 and 1^1G_4 configurations, the same Lorentz structure is adopted for their couplings to the $K\omega$ channel, while the corresponding effective coupling constants are treated independently. For the $K_4'(1G)$ state, the interaction Lagrangian is

$$\mathcal{L}_{K_4'(1G)\omega K} = g_{K_4'(1G)\omega K} K_4'^{+,\alpha\beta\gamma\delta} \omega_\alpha \partial_\beta \partial_\gamma \partial_\delta K^-. \quad (35)$$

Analogously, the $K_4(2210)K\omega$ interaction is described by

$$\mathcal{L}_{K_4(2210)\omega K} = g_{K_4(2210)\omega K} K_4^{+,\alpha\beta\gamma\delta} \omega_\alpha \partial_\beta \partial_\gamma \partial_\delta K^-. \quad (36)$$

For the spin-three state $K_3^*(1G)$, represented by the rank-three tensor field $K_3^{*,\alpha\beta\gamma}$, the $K\pi$ interaction contains three derivatives. Its effective Lagrangian is written as

$$\mathcal{L}_{K_3^*(1G)\pi K} = g_{K_3^*(1G)\pi K} K_3^{*+,\alpha\beta\gamma} [K^-(\partial_\alpha \partial_\beta \partial_\gamma \pi^0) - \pi^0(\partial_\alpha \partial_\beta \partial_\gamma K^-)]. \quad (37)$$

Combining the upper three-meson vertices with the exchanged-meson propagators and the lower meson–nucleon vertices, we obtain the tree-level t-channel amplitudes for the production of the $1G$-wave states. We use the same momentum convention as above, $q = p_1 - p_2 = k_2 - k_1$ and $t = q^2$.

For the $K_5^*(2380)$ production through pion exchange, the amplitude is

$$i\mathcal{M}_{K_5^*(2380)\pi K} = -g_{K_5^*(2380)\pi K} \frac{f_{\pi NN}}{m_\pi} \epsilon^{*,\sigma\alpha\beta\gamma\delta}(k_2) \frac{i}{t - m_\pi^2} \times (q_\sigma q_\alpha q_\beta q_\gamma q_\delta + k_{1\sigma} k_{1\alpha} k_{1\beta} k_{1\gamma} k_{1\delta}) \times q^\mu \bar{u}(p_2) \gamma_\mu \gamma_5 u(p_1) F_t(q). \quad (38)$$

For the $K_4'(1G)$ production, the retained ω-exchange contribution is

$$i\mathcal{M}_{K_4'(1G)\omega K} = -i g_{K_4'(1G)\omega K} \bar{u}(p_2) \left(g_{\omega NN} \gamma_\mu - \frac{i f_{\omega NN}}{2m_p} \sigma_{\nu\mu} q^\nu \right) u(p_1) \times \frac{-i}{t - m_\omega^2} \left(g_\alpha^\mu + \frac{q^\mu q_\alpha}{m_\omega^2} \right) \epsilon^{*,\alpha\beta\gamma\delta}(k_2) k_{1\beta} k_{1\gamma} k_{1\delta} F_t(q). \quad (39)$$

The $K_4(2210)$ amplitude has the same Lorentz structure, but involves the coupling constant associated with the $K_4(2210)$ state:

$$i\mathcal{M}_{K_4(2210)\omega K} = -i g_{K_4(2210)\omega K} \bar{u}(p_2) \left(g_{\omega NN} \gamma_\mu - \frac{i f_{\omega NN}}{2m_p} \sigma_{\nu\mu} q^\nu \right) u(p_1) \times \frac{-i}{t - m_\omega^2} \left(g_\alpha^\mu + \frac{q^\mu q_\alpha}{m_\omega^2} \right) \epsilon^{*,\alpha\beta\gamma\delta}(k_2) k_{1\beta} k_{1\gamma} k_{1\delta} F_t(q). \quad (40)$$

Finally, the $K_3^*(1G)$ production is dominated by the pion-exchange mechanism. The corresponding amplitude is

$$i\mathcal{M}_{K_3^*(1G)\pi K} = g_{K_3^*(1G)\pi K} \frac{f_{\pi NN}}{m_\pi} \bar{u}(p_2) \gamma_\alpha \gamma_5 u(p_1) q^\alpha \frac{i}{t - m_\pi^2} \times \epsilon^{*,\mu\nu\rho}(k_2)(q_\mu q_\nu q_\rho + k_{1\mu} k_{1\nu} k_{1\rho}) F_t(q). \quad (41)$$

In the above expressions, $\epsilon^{\mu\nu\rho\sigma\lambda}(k_2)$, $\epsilon^{\mu\nu\rho\sigma}(k_2)$, and $\epsilon^{\mu\nu\rho}(k_2)$ denote the polarization tensors of the produced spin-five, spin-four, and spin-three strange mesons, respectively. The quantities $\bar{u}(p_2)$ and $u(p_1)$ are the Dirac spinors of the outgoing and incoming nucleons. These amplitudes provide the ingredients required to evaluate the total and differential cross sections for the $1G$-wave states. For t-channel meson exchange, the form factor is adopted as

$$F_t(q) = \left(\frac{\Lambda_t^2 - m^2}{\Lambda_t^2 - q^2} \right)^2, \quad (42)$$

where m represents the mass of the exchanged particle. By fitting the available experimental cross-section data at different energies for the reaction $K^- p \to K_3^*(1780)p$ [14–16], we obtain $\Lambda_t = 1.5 \pm 0.2$ GeV, with $\chi^2/\text{d.o.f.} \leq 0.4$. Employing the same cutoff value for the $K^- p \to K_2(1820)p$ and $K^- p \to K_2(1770)p$ reactions, we find that the theoretical predictions are in good agreement with the measurements reported in Refs. [17,18,39].

The Regge trajectory model successfully describes hadron production at high energies [40,41]. Replacing the Feynman propagator with a Regge propagator effectively accounts for the exchange of high-spin and high-mass states in the t-channel, whose contributions become significant at higher energies. We implement Reggeization by substituting the t-channel Feynman propagators with Regge propagators [42], as follows:

$$\frac{1}{t - m_\pi^2} \to \left(\frac{s}{s_{\text{scale}}} \right)^{\alpha_\pi(t)} \frac{\pi \alpha_\pi'}{\Gamma[\alpha_\pi(t) + 1] \sin[\pi \alpha_\pi(t)]}, \quad (43)$$

$$\frac{1}{t-m_R^2} \to \left(\frac{s}{s_{\rm scale}}\right)^{\alpha_R(t)-1} \frac{\pi\alpha'_R}{\Gamma[\alpha_R(t)]\sin[\pi\alpha_R(t)]}; \quad (44)$$

the corresponding Regge trajectories for the exchanged mesons are

$$\alpha_R(t) = 1 + \alpha'_R(t - m_R^2), \qquad R = \rho, \omega, \quad (45)$$

$$\alpha_\pi(t) = \alpha'_\pi(t - m_\pi^2), \quad (46)$$

with slopes $\alpha'_\rho = 0.8\ \mathrm{GeV}^{-2}$, $\alpha'_\omega = 0.9\ \mathrm{GeV}^{-2}$, and $\alpha'_\pi = 0.7\ \mathrm{GeV}^{-2}$ [42].

Within the preceding theoretical framework, the cross sections for all reactions can be computed. The differential cross section in the c.m. frame is given by

$$\frac{d\sigma}{d\cos\theta_{\rm cm}} = \frac{1}{32\pi s}\frac{|\vec{k}_2^{\rm c.m.}|}{|\vec{k}_1^{\rm c.m.}|}\left(\frac{1}{2}\sum_\lambda |\mathcal{M}|^2\right), \quad (47)$$

where $s = (k_1 + p_1)^2$, and $\theta_{\rm cm}$ denotes the angle between the outgoing meson and the incoming K^- beam direction in the c.m. frame. The three-momenta $\vec{k}_1^{\rm c.m}$. and $\vec{k}_2^{\rm c.m}$. refer to the initial K^- beam and the final meson, respectively. The factor $1/2$ averages over the initial nucleon spin states.

III. NUMERICAL RESULTS AND DISCUSSIONS

Using the Lagrangians for the three-meson vertices introduced in the preceding section, we evaluate all relevant coupling constants, which are summarized in Table II. Decay widths used to determine the coupling constants are listed in Table III. With these couplings and the amplitude formulas given earlier, we compute the total and differential production cross sections for the $1D$-, $1F$-, and $1G$-wave states.

TABLE II. Coupling constants used in this work. The listed three-meson coupling constants are determined by fitting the decay widths from Refs. [20,23]. The meson-nucleon-nucleon coupling constants entering the lower vertices of the diagrams in Fig. 2 are taken from Ref. [33]. Couplings with mass dimensions are given with explicit units, while those without units are dimensionless.

$g_{K_3^*(1780)\pi K} = 3.84\ \mathrm{GeV}^{-2}$	$g_{K_3^*(1780)\rho K} = 12.36\ \mathrm{GeV}^{-3}$
$g_{K_2(1820)\omega K} = 5.85$	$g_{K_2(1820)\rho K} = 5.70$
$g_{K_2(1770)\omega K} = 5.93$	$g_{K_2(1770)\rho K} = 5.79$
$g_{K^*(1680)\pi K} = 1.76$	$g_{K_4^*(2045)\pi K} = 3.15\ \mathrm{GeV}^{-3}$
$g_{K_3'(2120)\omega K} = 3.02\ \mathrm{GeV}^{-1}$	$g_{K_3'(2120)\rho K} = 2.97\ \mathrm{GeV}^{-1}$
$g_{K_3(1F)\omega K} = 2.71\ \mathrm{GeV}^{-1}$	$g_{K_3(1F)\rho K} = 2.63\ \mathrm{GeV}^{-1}$
$g_{K_2^*(1980)\omega K} = 1.09\ \mathrm{GeV}^{-2}$	$g_{K_2^*(1980)\rho K} = 1.06\ \mathrm{GeV}^{-2}$
$g_{K_2^*(1980)\pi K} = 0.24\ \mathrm{GeV}^{-1}$	$g_{K_5^*(2380)\pi K} = 1.51\ \mathrm{GeV}^{-4}$
$g_{K_4'(1G)\omega K} = 2.13\ \mathrm{GeV}^{-2}$	$g_{K_4(2210)\omega K} = 2.09\ \mathrm{GeV}^{-2}$
$g_{K_3^*(1G)\pi K} = 0.33\ \mathrm{GeV}^{-2}$	

TABLE III. Decay widths used to determine the three-meson coupling constants in the present work. Experimental widths (denoted by superscript E) are taken from the PDG [7], while theoretical widths (denoted by superscript T) are adopted from Refs. [20,23] when corresponding experimental data are unavailable. All widths are given in MeV.

$\Gamma_{K_3^*(1780)\to\pi K} = 30.3^{\rm E}$	$\Gamma_{K_3^*(1780)\to\rho K} = 49.9^{\rm E}$
$\Gamma_{K_2(1820)\to\omega K} = 46.2^{\rm T}$	$\Gamma_{K_2(1820)\to\rho K} = 138.1^{\rm T}$
$\Gamma_{K_2(1770)\to\omega K} = 41.9^{\rm T}$	$\Gamma_{K_2(1770)\to\rho K} = 126.0^{\rm T}$
$\Gamma_{K^*(1680)\to\pi K} = 79.3^{\rm E}$	$\Gamma_{K_4^*(2045)\to\pi K} = 19.7^{\rm E}$
$\Gamma_{K_3'(2120)\to\omega K} = 6.7^{\rm T}$	$\Gamma_{K_3'(2120)\to\rho K} = 20.6^{\rm T}$
$\Gamma_{K_3(1F)\to\omega K} = 4.5^{\rm T}$	$\Gamma_{K_3(1F)\to\rho K} = 13.5^{\rm T}$
$\Gamma_{K_2^*(1980)\to\omega K} = 3.6^{\rm T}$	$\Gamma_{K_2^*(1980)\to\rho K} = 10.6^{\rm T}$
$\Gamma_{K_2^*(1980)\to\pi K} = 0.8^{\rm T}$	$\Gamma_{K_5^*(2380)\to\pi K} = 9.0^{\rm E}$
$\Gamma_{K_4'(1G)\to\omega K} = 2.3^{\rm T}$	$\Gamma_{K_4(2210)\to\omega K} = 1.5^{\rm T}$
$\Gamma_{K_3^*(1G)\to\pi K} = 1.04^{\rm T}$	

A. Analysis of 1D-wave kaon production

As shown in Fig. 3, we first analyze the total cross section of the $K^-p \to K_3^*(1780)p$ reaction. In the calculation, both the π- and ρ-exchange contributions are included, as indicated in the figure. It can be seen that the π exchange gives the dominant contribution to the total cross section, while the ρ exchange only provides a relatively small correction. In fitting the experimental total cross sections, the only adjustable parameter is the cutoff parameter Λ_t in the form factor. The best description of the data is obtained with $\Lambda_t = 1.5$ GeV, and the theoretical uncertainty band is generated by varying this value by

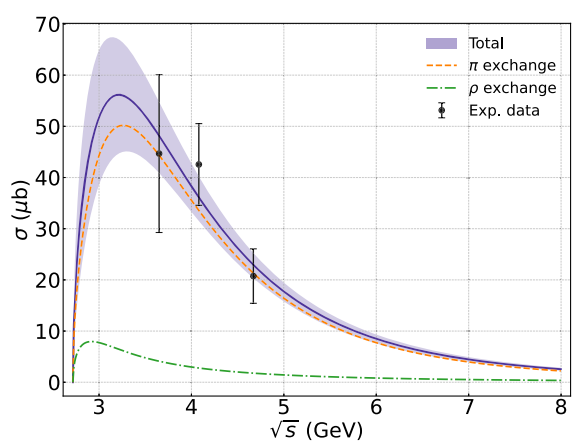

FIG. 3. Calculated total production cross section for the $K_3^*(1780)$ state, along with comparisons to experimental data. The experimental data are taken from Refs. [14–16]. All error bands and the solid lines within them correspond to results obtained with the cutoff parameter set to 1.5 ± 0.2 GeV.

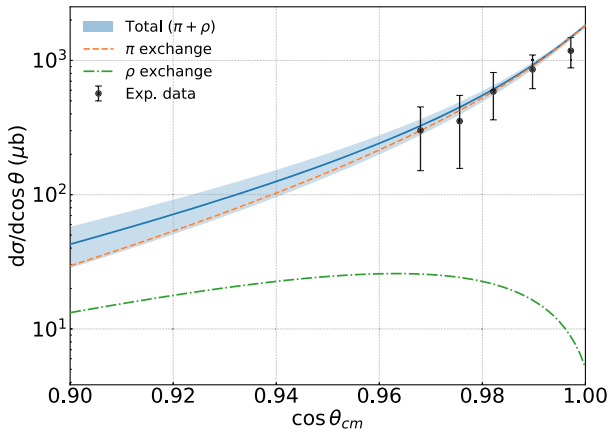

FIG. 4. Calculated differential production cross section for the $K_3^*(1780)$ state, along with comparisons to experimental data. The differential cross section is evaluated at a c.m. energy of 4.08 GeV. The experimental data are taken from Ref. [15]. The error bands and the solid lines within them represent results obtained with the cutoff parameter set to 1.5 ± 0.2 GeV. Since the available differential cross-section data are concentrated at small forward angles, our theoretical predictions are also presented only in this angular region.

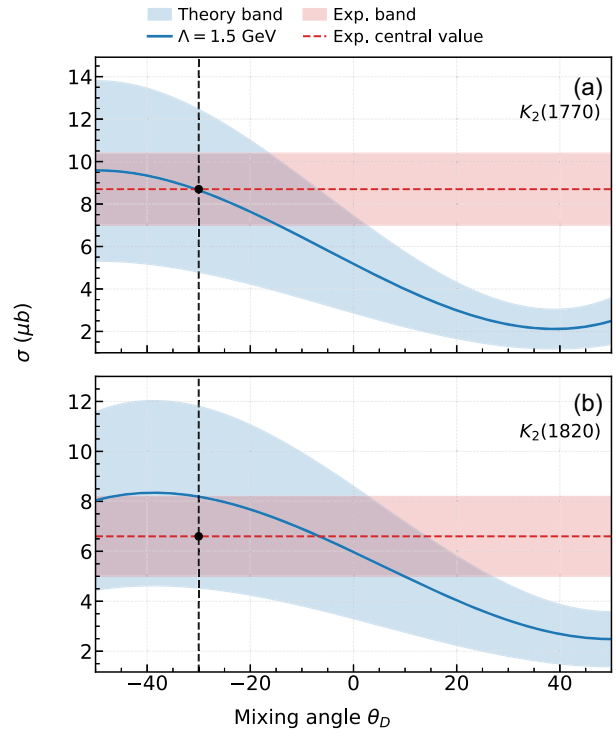

FIG. 5. Total cross sections for the reactions $K^-p \to K_2(1770)p$ and $K^-p \to K_2(1820)p$ as functions of the $K_2(1770)$–$K_2(1820)$ mixing angle. The vertical dashed line denotes the mixing angle $\theta_{1D} = -30°$ adopted in the numerical calculations. In panel (a), the red band represents the experimental value $\sigma[K^-p \to K_2(1770)p] = 8.7 \pm 1.7$ μb at $\sqrt{s} = 4.67$ GeV. In panel (b), the red band represents the experimental value $\sigma[K^-p \to K_2(1820)p] = 6.6 \pm 1.6$ μb at the same c.m. energy.

± 0.2 GeV. With this single parameter, the calculated total cross section can reproduce the available experimental measurements over the considered energy region, especially around the energy range, where the data are concentrated.

For the second experimental point of the total cross section in Fig. 3, corresponding to the c.m. energy $\sqrt{s} = 4.08$ GeV, differential cross-section data are also available. Based on this experimental information, we further compare our theoretical result with the measured angular distribution in Fig. 4. The same cutoff parameter $\Lambda_t = 1.5 \pm 0.2$ GeV, fixed from the total cross-section fit, is used to evaluate the differential cross section.[3] The resulting angular distribution agrees well with the experimental data in the forward-angle region. The calculation also shows a clear forward-peaked behavior, which is a typical feature of the t-channel exchange process. Such a simultaneous description of both the total and differential cross sections supports the reliability of the present effective Lagrangian model for the $K_3^*(1780)$ production.

For the production of the $K_2(1770)$ state, the dependence of the total cross section on the $K_2(1770)$–$K_2(1820)$ mixing angle is first examined, as shown in Fig. 5. Since these two physical states arise from the spin mixing between the 1^3D_2 and 1^1D_2 configurations, the corresponding three-meson coupling constants are sensitive to the mixing angle through the strong decay widths. Previous studies of their strong decay behaviors suggested that the mixing angle prefers a negative value [20]. Motivated by this observation, we calculate the total production cross section as a function of the mixing angle. For the reaction $K^-p \to K_2(1770)p$, the experimental total cross section at $\sqrt{s} = 4.67$ GeV is 8.7 ± 1.7 μb. The best agreement between the theoretical prediction and the experimental value is obtained around $\theta_{1D} = -30°$, as indicated by the vertical dashed line in Fig. 5(a). This result supports the negative mixing angle favored by the strong decay analysis and provides an independent constraint from the production process.

With the same mixing angle $\theta_{1D} = -30°$, we further analyze the total production cross section of the $K_2(1820)$ state. The experimental value for $K^-p \to K_2(1820)p$ at $\sqrt{s} = 4.67$ GeV is 6.6 ± 1.6 μb. As shown in Fig. 5(b), the theoretical prediction obtained at the same mixing angle also lies within the experimental uncertainty band, indicating that a unified choice of the mixing angle can simultaneously describe the measured total cross sections of both $K_2(1770)$ and $K_2(1820)$. This agreement is meaningful because the two states are described by the same mixing

[3]Before closing this section, we want to indicate the theoretical uncertainties in our predictions. The calculated cross sections depend not only on the fitted parameters but also on phenomenological factors, such as the form factors, coupling constants, and neglected exchange mechanisms.

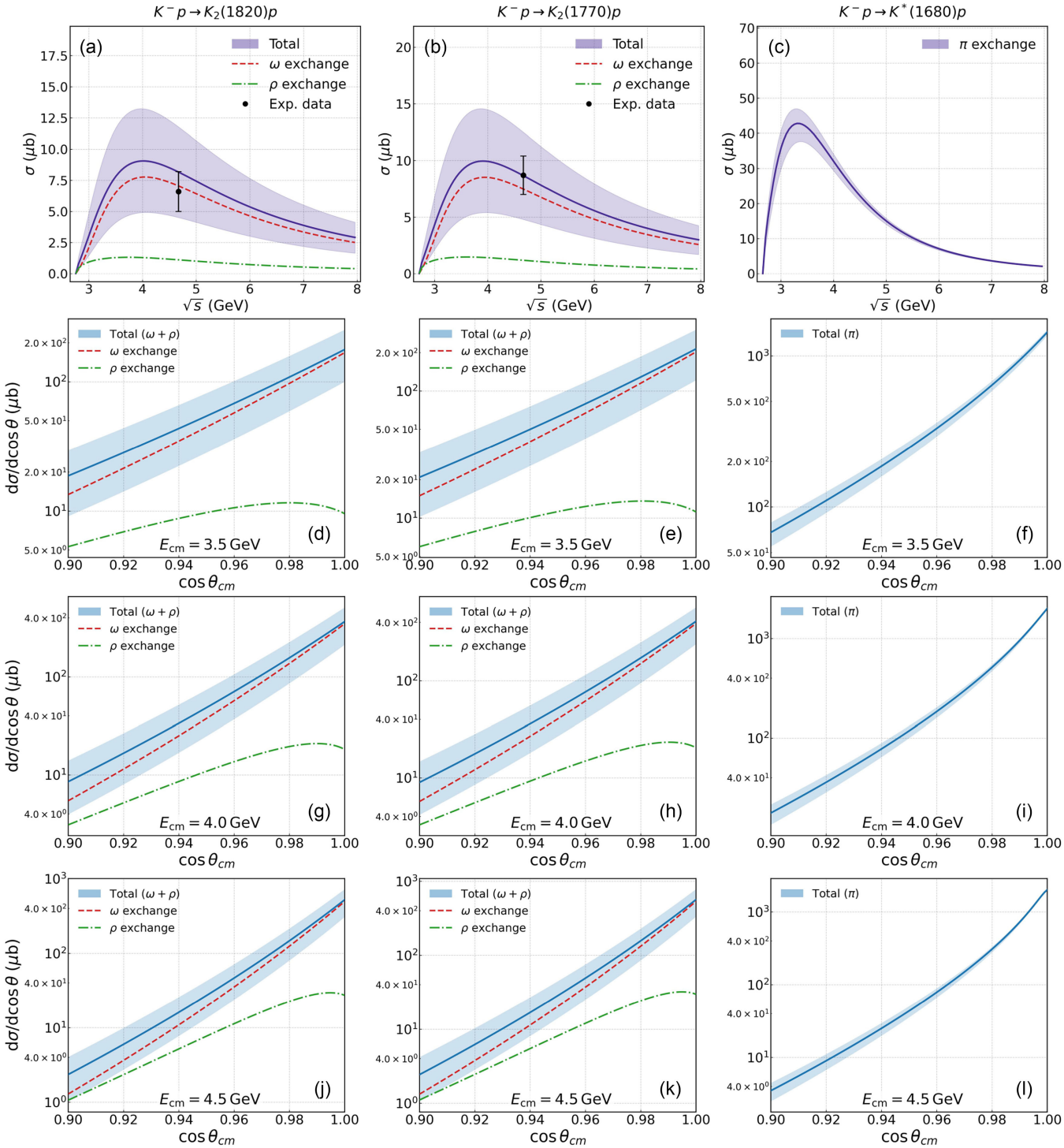

FIG. 6. Calculated total and differential production cross sections for the $1D$-wave states [$K_2(1820)$, $K_2(1770)$, and $K^*(1680)$], along with comparisons to experimental data. Panels (a)–(c) show the corresponding total cross sections, while panels (d)–(f), (g)–(i), and (j)–(l) show the differential cross sections at E_{cm} = 3.5, 4.0, and 4.5 GeV, respectively. The experimental data are taken from Refs. [17,18,39]. In all figures, the error bands and the solid lines within them represent results obtained with the cutoff parameter set to 1.5 ± 0.2 GeV. Because the differential cross section are concentrated in the small forward-angle region, only the angular range close to $\cos\theta_{\rm cm} = 1$ is shown.

angle, but their production processes depend on different coupling constants. After fixing the mixing angle, the corresponding coupling constants are used to calculate the energy-dependent total cross sections shown in the left two columns of Fig. 6. In these calculations, both ρ- and ω-exchange contributions are included. The ω exchange gives the dominant contribution, while the ρ exchange provides a smaller correction, and their coherent contribution reproduces the available experimental data reasonably well.

The differential cross sections for the $K^-p \to K_2(1770)p$ reaction are displayed in Figs. 6(e), 6(h), and 6(k) at several c.m. energies. The angular distributions are presented in the forward region, where experimental measurements are available and where the t-channel exchange mechanism is expected to be most important. A clear forward-peaked behavior appears as $\cos\theta_{\rm cm}$ approaches unity, which is a typical feature of meson exchange in the t channel. The total differential distribution is mainly governed by the ω-exchange contribution, while the ρ-exchange contribution remains smaller over the considered angular range. The uncertainty bands caused by the cutoff parameter variation show that the forward enhancement remains almost unchanged within the model uncertainty. Therefore, the differential behavior of the $K_2(1770)$ production further supports the dominance of the t-channel mechanism used in the present calculation.

For the $K^-p \to K_2(1820)p$ reaction, the differential cross sections shown in Figs. 6(d), 6(g), and 6(j) exhibit a pattern similar to that of the $K_2(1770)$ state. The distributions increase rapidly toward the forward-angle region, again reflecting the characteristic behavior of the t-channel ρ- and ω-exchange processes. The ω exchange provides the leading contribution, whereas the ρ exchange gives a relatively small but visible correction. Since the coupling constants used here are determined at the mixing angle $\theta_{1D} = -30°$, which has already been constrained by the total cross sections of both the $K_2(1770)$ and $K_2(1820)$, the differential predictions in Fig. 6 can be regarded as a direct consequence of the same mixing-angle scheme. The simultaneous description of the total and differential cross sections for these two $1D$-wave kaons demonstrates that the present effective Lagrangian model provides a coherent picture for their production in the K^-p reaction.

For the production of the $K^*(1680)$ state, the calculated total cross section is shown in Fig. 6(c). In contrast to the $K_2(1770)$ and $K_2(1820)$ cases, only the π-exchange contribution is retained in the final result for the $K^-p \to K^*(1680)p$ reaction, since the contributions from other possible exchanged mesons are found to be negligibly small. With the same cutoff parameter $\Lambda_t = 1.5 \pm 0.2$ GeV used for the other $1D$-wave states, the total cross section rises rapidly from the threshold region, reaches a sizable maximum at low c.m. energies, and then decreases gradually with increasing $\sqrt{s}$.

The corresponding differential cross sections for the $K^-p \to K^*(1680)p$ reaction are displayed in Figs. 6(f), 6(i), and 6(l) at $\sqrt{s} = 3.5$, 4.0, and 4.5 GeV, respectively. A pronounced forward enhancement is observed in all three angular distributions, with the differential cross section increasing rapidly as $\cos\theta_{\rm cm}$ approaches unity. Compared with the $K_2(1770)$ and $K_2(1820)$ cases, the forward-angle differential cross section of the $K^*(1680)$ channel is relatively large, reflecting its strong coupling to the $K\pi$ mode. The uncertainty bands generated by varying the cutoff parameter remain moderate and do not change the forward-peaked structure. Therefore, the combined description of the total and differential cross sections suggests that the present effective Lagrangian framework gives a consistent account of the $K^*(1680)$ production mechanism.

B. Analysis of 1F-wave kaon production

For the $K^-p \to K_4^*(2045)p$ reaction, the production is evaluated through the t-channel π-exchange mechanism. As shown in the first column of Fig. 7, the calculated total cross section rises rapidly from the threshold region and reaches a maximum of about 25.6 μb, after which it decreases gradually with increasing $\sqrt{s}$. The only available experimental measurement is located at $\sqrt{s} = 4.08$ GeV, with $\sigma_{\rm exp} = 36.4 \pm 12.1$ μb [18]. Although the theoretical curve is lower than the central value of this experimental point, the predicted value lies close to the lower edge of the experimental uncertainty band.

The corresponding differential cross sections for $K^-p \to K_4^*(2045)p$ are calculated at $\sqrt{s} = 3.5$, 4.0, and 4.5 GeV, as displayed in the lower panels of the first column of Fig. 7. A pronounced forward-peaked behavior appears at all three energies, with $d\sigma/d\cos\theta_{\rm cm}$ increasing rapidly as $\cos\theta_{\rm cm}$ approaches unity. At $\sqrt{s} = 3.5$ GeV, the distribution already shows a clear forward enhancement and reaches about 10^2 μb near the forward end. When the energy increases to $\sqrt{s} = 4.0$ GeV, the angular distribution becomes steeper, and the forward differential cross section is further enhanced. At $\sqrt{s} = 4.5$ GeV, although the total cross section has started to decrease, the differential cross section is more strongly concentrated in the very forward region and reaches the order of 10^3 μb as $\cos\theta_{\rm cm} \to 1$. Therefore, the production of the $K_4^*(2045)$ is expected to be most visible in the forward-angle region, which provides a useful guide for future measurements of this $1F$-wave kaon state in K^-p scattering experiments [12].

The recently observed $K_3'(2120)$ state deserves particular attention, since the available experimental analysis has established its resonance parameters but has not yet provided information on its production cross section [13]. The decay calculation supports its assignment as a $1F$-wave kaon. The predicted total width is consistent with the experimental result [13]. The present production analysis therefore provides complementary information that can be

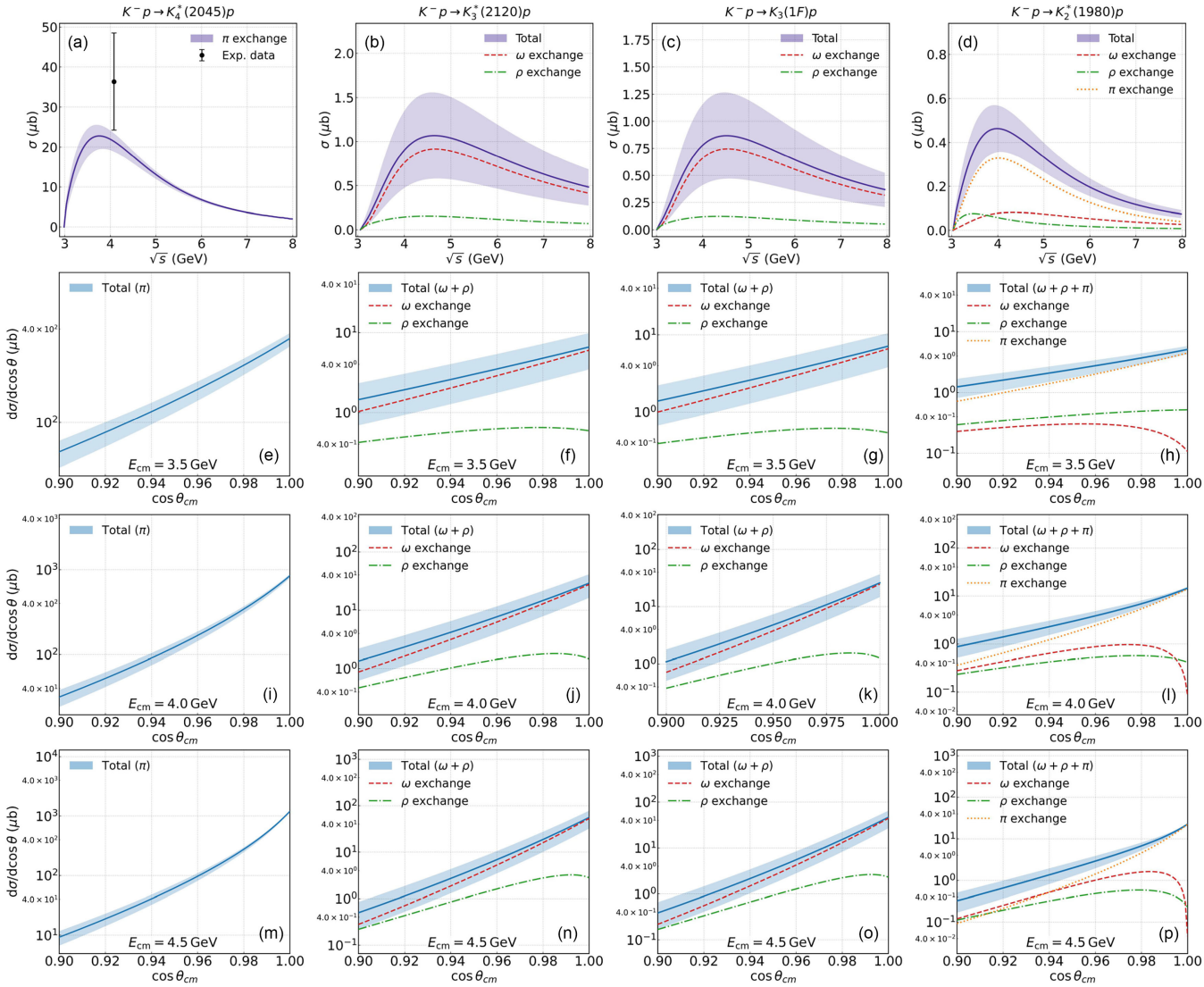

FIG. 7. Calculated total and differential production cross sections for the $1F$-wave states [$K_4^*(2045)$, $K_3'(2120)$, $K_3(1F)$, and $K_2^*(1980)$]. Panels (a)–(d) show the corresponding total cross sections, while panels (e)–(h), (i)–(l), and (m)–(p) show the differential cross sections at $E_{cm} = 3.5$, 4.0, and 4.5 GeV, respectively. The experimental data are taken from Ref. [18]. In all figures, the error bands and the solid lines within them represent results obtained with the cutoff parameter set to 1.5 ± 0.2 GeV. Because the differential cross sections are concentrated in the small forward-angle region, only the angular range close to $\cos\theta_{\rm cm} = 1$ is shown.

used to design a dedicated search in the K^-p reaction. As shown in Fig. 7(b), the total cross section for $K^-p \to K_3'(2120)p$ rises rapidly above threshold and develops a broad maximum around $\sqrt{s} \simeq 4.5$ GeV. Within the adopted cutoff variation, the upper edge of the theoretical band reaches approximately 1.6 μb, while the central curve is close to 1.1 μb at the maximum. The decomposition of the result indicates that the ω-exchange contribution determines the overall magnitude and energy dependence, whereas the ρ exchange provides a smaller correction. The differential distributions in Figs. 7(f), 7(j), and 7(n) reveal an additional feature. At $\sqrt{s} = 3.5$ GeV, the cross section already increases toward the forward direction and reaches several μb as $\cos\theta_{\rm cm} \to 1$. At $\sqrt{s} = 4.0$ GeV, the forward yield increases to the order of 10 μb, and at $\sqrt{s} = 4.5$ GeV it reaches several tens of μb in the most forward angular region. Meanwhile, the enhancement away from the extreme forward region is much less pronounced. Consequently, a measurement with sufficient acceptance close to $\cos\theta_{\rm cm} = 1$ would provide a useful and experimentally testable strategy for confirming the $K_3'(2120)$ state.

The unobserved $K_3(1F)$ state is the spin-mixing partner of the $K_3'(2120)$ and can be investigated within the same experimental setup. The production result in Fig. 7(c) exhibits an energy dependence similar to that of the $K_3'(2120)$. The total cross section reaches a broad maximum in the same energy region, with the upper edge of

the theoretical uncertainty band approaching 1.25 μb and the central prediction remaining around 0.9 μb. As in the $K_3'(2120)$ channel, the ω exchange gives the leading contribution, whereas the ρ-exchange component is subdominant. The differential cross sections displayed in Figs. 7(g), 7(k), and 7(o) show that the angular distribution becomes increasingly concentrated near the forward limit as the c.m. energy is raised from 3.5 to 4.5 GeV. Near $\cos\theta_{\rm cm} = 1$, the predicted differential cross section increases from several μb at $\sqrt{s} = 3.5$ GeV to the order of 10 μb at $\sqrt{s} = 4.0$ GeV, and then to several tens of μb at $\sqrt{s} = 4.5$ GeV. The close similarity between the angular distributions of the two mixed $1F$ states implies that the production angle alone may not be sufficient to separate them. A complementary analysis of the invariant-mass spectra and their decay properties would provide a more discriminating test of the proposed spin-mixing scenario.

For the $K^-p \to K_2^*(1980)p$ reaction, the predicted total cross section is shown in Fig. 7(d). In this calculation, the ω-, ρ-, and π-exchange mechanisms are all taken into account, which makes this channel different from several other $1F$-wave states where only one or two exchanged mesons give sizable contributions. The total cross section rises rapidly from threshold and reaches its maximum value around $\sqrt{s} \simeq 3.8$–4.0 GeV, with the central theoretical peak being about 0.5 μb. After the peak, the cross section decreases gradually as the c.m. energy increases. The decomposition of the total result indicates that the π-exchange contribution is the largest one, while the ω and ρ exchanges also give visible but smaller contributions. This feature is especially interesting because, as shown in Table III, the partial width of the $K_2^*(1980) \to \pi K$ channel is much smaller than those of the ρK and ωK channels. Therefore, the production strength is not determined only by the decay width; it is also strongly affected by the light pion propagator, the πNN coupling, and the momentum dependence of the t-channel amplitude. Compared with the $1D$-wave kaon production shown in Fig. 6, the overall magnitude of the $1F$-wave kaon production is evidently reduced, which is consistent with the general tendency that the production cross section becomes smaller when the orbital angular momentum of the produced state increases.

The corresponding differential cross sections for $K^-p \to K_2^*(1980)p$ are displayed in Figs. 7(h), 7(l), and 7(p) at $\sqrt{s} = 3.5$, 4.0, and 4.5 GeV, respectively. At all three energies, the angular distributions exhibit a clear forward enhancement. At $\sqrt{s} = 3.5$ GeV, the differential cross section is relatively moderate and reaches only several μb in the very forward region. When the energy increases to $\sqrt{s} = 4.0$ GeV, the angular distribution becomes steeper, and the forward differential cross section increases to the order of 10 μb. At $\sqrt{s} = 4.5$ GeV, although the total cross section has already started to decrease from its peak region, the differential distribution is more concentrated near $\cos\theta_{\rm cm} = 1$, and the forward value remains at the order of 10 μb. In these three panels, the π-exchange contribution grows most rapidly toward the forward direction and dominates the total result, while the ω- and ρ-exchange contributions remain non-negligible corrections. Thus, the forward-angle region provides the most favorable kinematic window for searching for the $K_2^*(1980)$ production in future K^-p scattering measurements [12].

C. Analysis of 1G-wave kaon production

For the $K^-p \to K_5^*(2380)p$ reaction, the production process is dominated by the t-channel π-exchange mechanism, as shown in Fig. 8(a). The calculated total cross section increases rapidly from the threshold region and reaches its maximum value of about 6.5 μb around $\sqrt{s} \simeq 4.4$ GeV. After the peak, the cross section decreases gradually with increasing c.m. energy and decreases to about 2 μb at $\sqrt{s} = 7.0$ GeV. Among the four $1G$-wave states considered here, the $K_5^*(2380)$ channel gives the largest total cross section. Nevertheless, compared with the $1D$- and $1F$-wave kaon productions discussed above, its magnitude is still reduced. This behavior supports the general tendency that the production cross section decreases as the orbital angular momentum of the produced kaon state increases, namely the overall hierarchy $\sigma_{1G} < \sigma_{1F} < \sigma_{1D}$.

The corresponding differential cross section for $K^-p \to K_5^*(2380)p$ is displayed in Fig. 8(e), where the results at $\sqrt{s} = 3.5$, 4.0, and 4.5 GeV are shown together. A clear forward-peaked structure appears at all three energies, which is the typical feature of the t-channel exchange process. Near $\cos\theta_{\rm cm} = 1$, the differential cross section is only at the order of 10 μb for $\sqrt{s} = 3.5$ GeV, while it increases to the order of 10^2 μb at $\sqrt{s} = 4.0$ GeV. At $\sqrt{s} = 4.5$ GeV, where the total cross section is close to its peak region, the angular distribution becomes much steeper and the forward differential cross section can reach several 10^2 μb. Therefore, although the integrated production rate of this $1G$-wave state is smaller than those of the lower-orbital kaons, the very forward region still provides a favorable kinematic window for searching for the $K_5^*(2380)$ in future K^-p measurements [12].

For the $K^-p \to K_4'(1G)p$ reaction, the calculated total cross section is presented in Fig. 8(b). In this channel, only the ω-exchange contribution is retained in the final calculation, because the other possible exchanged-meson contributions are found to be strongly suppressed. This is different from the mixed $1D$-wave states $K_2(1770)$ and $K_2(1820)$, as well as the mixed $1F$-wave states $K_3'(2120)$ and $K_3(1F)$, where both ρ- and ω-exchange mechanisms were included. The total cross section of $K_4'(1G)$ rises from threshold and develops a broad maximum around $\sqrt{s} \simeq 5.0$ GeV. The central value of the peak is approximately 0.32 μb, with a sizable uncertainty band induced by the cutoff parameter. This magnitude is much smaller than that of the $K_5^*(2380)$ channel and is also below the

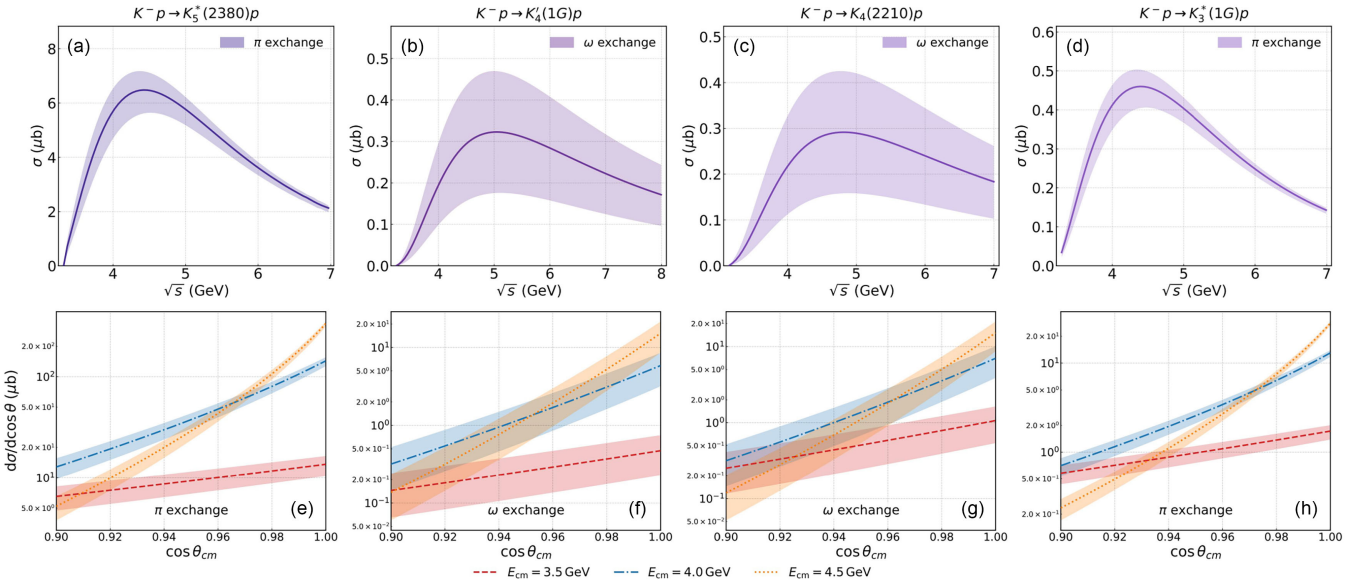

FIG. 8. Calculated total and differential production cross sections for the $1G$-wave strange meson states $K_5^*(2380)$, $K_4'(1G)$, $K_4(2210)$, and $K_3^*(1G)$ in the K^-p reaction. Panels (a)–(d) show the total cross sections as functions of the c.m. energy $\sqrt{s}$, while panels (e)–(h) present the corresponding differential cross sections $d\sigma/d\cos\theta_{\rm cm}$ in the forward-angle region. The differential cross sections are evaluated at $E_{\rm cm} = 3.5$, 4.0, and 4.5 GeV. From left to right, the four columns correspond to the production of $K_5^*(2380)$, $K_4'(1G)$, $K_4(2210)$, and $K_3^*(1G)$, respectively. The shaded bands denote the theoretical uncertainties induced by varying the cutoff parameter within $\Lambda_t = 1.5 \pm 0.2$ GeV, while the solid curves represent the central predictions with $\Lambda_t = 1.5$ GeV. Because the differential cross sections are concentrated in the small forward-angle region, only the angular range close to $\cos\theta_{\rm cm} = 1$ is shown.

typical production scale of the $1F$-wave mixed states, reflecting the suppression associated with the higher orbital excitation.

The differential cross section for $K^-p \to K_4'(1G)p$ is shown in Fig. 8(f). The angular distributions at $\sqrt{s} = 3.5$, 4.0, and 4.5 GeV all increase toward the forward direction. At $\sqrt{s} = 3.5$ GeV, the forward differential cross section is relatively small and is below 1 μb near $\cos\theta_{\rm cm} = 1$. When the energy is raised to $\sqrt{s} = 4.0$ GeV, the forward value increases to several μb. At $\sqrt{s} = 4.5$ GeV, the distribution becomes more strongly concentrated near $\cos\theta_{\rm cm} = 1$, and the forward differential cross section reaches the order of 10 μb.

For the newly observed $K_4(2210)$ state, the total production cross section of the $K^-p \to K_4(2210)p$ reaction is shown in Fig. 8(c). Since $K_4(2210)$ is a newly reported strange meson, its production prediction is particularly important for future confirmation of this state in kaon-beam experiments [12]. Similar to its mixed partner $K_4'(1G)$, only the ω-exchange mechanism is included in the calculation, because the ρ-exchange and other possible contributions are numerically very small. The predicted total cross section of the $K_4(2210)$ reaches a broad maximum of about 0.29 μb around $\sqrt{s} \simeq 4.8$–5.0 GeV and then decreases slowly as $\sqrt{s}$ increases. Its production strength is comparable to that of $K_4'(1G)$.

The corresponding angular distributions for $K^-p \to K_4(2210)p$ are displayed in Fig. 8(g). At $\sqrt{s} = 3.5$ GeV, the differential cross section is relatively weak over the whole forward-angle region and reaches about 1 μb near $\cos\theta_{\rm cm} = 1$. At $\sqrt{s} = 4.0$ GeV, the forward yield increases to several μb. When the energy becomes $\sqrt{s} = 4.5$ GeV, the angular distribution grows more rapidly as $\cos\theta_{\rm cm}$ approaches unity, and the forward value reaches the order of 10 μb. The curves at different energies also show that the higher-energy distribution is more strongly compressed into the very forward region.

For the $K^-p \to K_3^*(1G)p$ reaction, the total cross section is plotted in Fig. 8(d). The production is evaluated through the dominant π-exchange mechanism, while the contributions from other possible exchanged mesons are neglected because they are much smaller in the numerical calculation. The total cross section rises quickly from threshold and reaches a maximum of about 0.46 μb around $\sqrt{s} \simeq 4.4$ GeV. After the peak, the cross section decreases continuously with increasing energy.

The differential cross section for $K^-p \to K_3^*(1G)p$ is presented in Fig. 8(h). Similar to the other $1G$-wave channels, the angular distributions at $\sqrt{s} = 3.5$, 4.0, and 4.5 GeV exhibit an evident forward enhancement. At $\sqrt{s} = 3.5$ GeV, the forward differential cross section is only at the level of a few μb. At $\sqrt{s} = 4.0$ GeV, it increases to the order of 10 μb near $\cos\theta_{\rm cm} = 1$. At $\sqrt{s} = 4.5$ GeV,

the distribution becomes the steepest among the three energies and the forward value can reach several tens of μb.

It should be noted that, as shown in Figs. 6 and 7, the available experimental data in this reaction channel and energy region remain rather limited, mainly due to the significant experimental challenges involved. Compared with Figs. 3 and 4, where data are more abundant, the number of experimental reference points in Figs. 6 and 7 is considerably smaller. Nevertheless, we argue that these limited data still carry important value. On the one hand, precisely because of the scarcity of experimental information in this energy regime, our theoretical calculations can serve as a useful reference and provide predictions for future meson-beam experiments. On the other hand, our model is able to reasonably reproduce the main energy-dependent trends exhibited by these few data points, and this qualitative agreement lends some support to the viability of our model framework. Furthermore, this conclusion is reinforced by the good agreement between theory and experiment shown in Figs. 3 and 4 in the better-constrained energy regions, which together bolsters the reliability of our overall theoretical description.

IV. SUMMARY

In this work, we have systematically investigated the production of high-orbital kaon excitations in the K^-p reaction, with emphasis on the $1D$-, $1F$-, and $1G$-wave strange-meson states. Within the effective Lagrangian model, the dominant t-channel exchange mechanisms were constructed for the relevant production processes. The exchanged mesons were selected according to the dominant kaon-containing decay channels of the produced states. In addition, the finite-size effects at the interaction vertices were taken into account by introducing a phenomenological form factor. The cutoff parameter was determined to be $\Lambda_t = 1.5 \pm 0.2$ GeV by fitting the available experimental data for the $K^-p \to K_3^*(1780)p$ reaction. With the same value of Λ_t, the production of other high-orbital kaon states was further studied without introducing additional free parameters.

For the $1D$-wave kaons, the available experimental data for the $K_3^*(1780)$, $K_2(1770)$, and $K_2(1820)$ are used to constrain and test the present model. The production of the $K^*(1680)$ is then evaluated with the same parameter set, and its total cross section and angular distributions are presented as theoretical predictions, since no direct experimental production cross-section data are available in the considered energy region.

Using the same theoretical framework, we further predicted the production cross sections of the $1F$- and $1G$-wave kaon states. The obtained result for the $K_4^*(2045)$ is compatible with the available experimental information. Predictions were also made for $K_3'(2120)$, $K_3(1F)$, $K_2^*(1980)$, $K_5^*(2380)$, $K_4'(1G)$, $K_4(2210)$, and $K_3^*(1G)$. These results provide useful theoretical guidance for the search for poorly established or still-unobserved high-orbital kaon states. Although the production strength generally decreases with increasing orbital excitation, the predicted cross sections remain sizable. Moreover, the differential cross sections are mainly concentrated in the forward-angle region, suggesting that forward-angle measurements are especially favorable for observing these excited strange mesons.

Overall, the present study provides a unified description of high-orbital kaon production in K^-p scattering within the effective Lagrangian model. The successful reproduction of existing experimental data and the extension to the less-explored $1F$- and $1G$-wave sectors demonstrate the reliability and predictive power of this framework. These results not only improve our understanding of the production dynamics of excited kaons, but also provide valuable theoretical references for future kaon-beam experiments at facilities such as J-PARC and other high-intensity meson-beam programs.

ACKNOWLEDGMENTS

This work is supported by the Natural Science Foundation of Gansu Province (Grants No. 26RCKA012 and No. 25JRRA799), the National Natural Science Foundation of China under Grants No. 12335001 and No. 12247101, the "111 Center" under Grant No. B20063, the Fundamental Research Funds for the Central Universities (Grant No. lzujbky-2023-stlt01), and Lanzhou City High-Level Talent Funding.

DATA AVAILABILITY

The data that support the findings of this article are openly available [7], embargo periods may apply.

[1] H.-X. Chen, W. Chen, X. Liu, Y.-R. Liu, and S.-L. Zhu, Rep. Prog. Phys. **86**, 026201 (2023).
[2] Z.-Y. Bai, D.-Y. Chen, Qi-Huang, X. Liu, S.-Q. Luo, and J.-Z. Wang, arXiv:2602.19887.
[3] X. Wang, X. Liu, and Y. Gao, Rev. Mod. Phys. **98**, 021001 (2026).
[4] M. Ablikim *et al.* (BESIII Collaboration), J. High Energy Phys. 01 (2024) 180.
[5] B. Aubert *et al.* (*BABAR* Collaboration), Phys. Rev. D **77**, 092002 (2008).
[6] A. V. Anisovich, C. A. Baker, C. J. Batty, D. V. Bugg, C. Hodd, H. C. Lu, V. A. Nikonov, A. V. Sarantsev, V. V. Sarantsev, and B. S. Zou, Phys. Lett. B **491**, 47 (2000).
[7] S. Navas *et al.* (Particle Data Group), Phys. Rev. D **110**, 030001 (2024).
[8] T.-Y. Li, Z.-Y. Bai, and X. Liu, Phys. Rev. D **113**, 054050 (2026).
[9] X.-Y. Wang and J. He, Eur. Phys. J. A **55**, 152 (2019).
[10] X.-Y. Wang and J. He, Phys. Rev. D **96**, 034017 (2017).
[11] X.-Y. Wang, H.-F. Zhou, and X. Liu, Phys. Rev. D **108**, 034015 (2023).
[12] X. WANG and X. LIU, Nucl. Phys. Rev. **42**, 10 (2025).
[13] G. D. Alexeev *et al.* (COMPASS Collaboration), arXiv: 2504.09470.
[14] P. F. Bird, Cherenkov ring imaging and spectroscopy of charged K^* interactions at 11-GeV/c, Ph.D. thesis, Stanford University, SLAC Report No. 332 (1989).
[15] M. Baubillier *et al.* (Birmingham-CERN-Glasgow-Michigan State-Paris Collaboration), Z. Phys. C **26**, 37 (1984).
[16] S. Toaff *et al.*, Phys. Rev. D **23**, 1500 (1981).
[17] D. Aston *et al.*, Phys. Lett. B **308**, 186 (1993).
[18] M. Baubillier *et al.* (Birmingham-CERN-Glasgow-Michigan State-Paris Collaboration), Phys. Lett. **118B**, 447 (1982).
[19] T.-y. Li, Y.-r. Wang, and C.-q. Pang, Phys. Rev. D **107**, 074008 (2023).
[20] C.-Q. Pang, J.-Z. Wang, X. Liu, and T. Matsuki, Eur. Phys. J. C **77**, 861 (2017).
[21] S. Jafarzade, A. Vereijken, M. Piotrowska, and F. Giacosa, Phys. Rev. D **106**, 036008 (2022).
[22] S. Jafarzade, A. Koenigstein, and F. Giacosa, Phys. Rev. D **103**, 096027 (2021).
[23] Y.-R. Wang, H. Chen, X.-H. Liu, and C.-Q. Pang, Phys. Rev. D **112**, 094039 (2025).
[24] M. Piotrowska, C. Reisinger, and F. Giacosa, Phys. Rev. D **96**, 054033 (2017).
[25] V. Shastry, C. S. Fischer, and F. Giacosa, Phys. Lett. B **834**, 137478 (2022).
[26] R. Baldi, T. Bohringer, P. A. Dorsaz, V. Hungerbuhler, M. N. Kienzle-Focacci, M. Martin, A. Mermoud, C. Nef, and P. Siegrist, Phys. Lett. B **63**, 344 (1976).
[27] E. Konigs *et al.*, Phys. Lett. **74B**, 282 (1978).
[28] S. U. Chung *et al.*, Phys. Rev. Lett. **40**, 355 (1978).
[29] D. Aston *et al.*, Nucl. Phys. **B296**, 493 (1988).
[30] D. Aston *et al.*, Nucl. Phys. **B292**, 693 (1987).
[31] C. Daum *et al.* (ACCMOR Collaboration), Nucl. Phys. **B187**, 1 (1981).
[32] R. Aaij *et al.* (LHCb Collaboration), Phys. Rev. Lett. **118**, 022003 (2017).
[33] T. A. Rijken, M. M. Nagels, and Y. Yamamoto, Prog. Theor. Phys. Suppl. **185**, 14 (2010).
[34] M. M. Nagels, T. A. Rijken, and Y. Yamamoto, Phys. Rev. C **99**, 044003 (2019).
[35] M. Ablikim *et al.* (BESIII Collaboration), Phys. Rev. D **100**, 032004 (2019).
[36] D. Aston *et al.*, Phys. Lett. **106B**, 235 (1981).
[37] D. Aston *et al.*, Phys. Lett. B **180**, 308 (1986); **183**, 434(E) (1987).
[38] M. Ablikim *et al.* (BESIII Collaboration), Phys. Rev. D **101**, 032008 (2020).
[39] P. Estabrooks, R. K. Carnegie, A. D. Martin, W. M. Dunwoodie, T. A. Lasinski, and D. W. G. S. Leith, Nucl. Phys. **B133**, 490 (1978).
[40] S. Ozaki, H. Nagahiro, and A. Hosaka, Phys. Rev. C **81**, 035206 (2010).
[41] J. K. Storrow, Phys. Rep. **103**, 317 (1984).
[42] M. Guidal, J. M. Laget, and M. Vanderhaeghen, Nucl. Phys. **A627**, 645 (1997).